Maximum Thrust Studies of an Isolated Rotor with CFD Turbulence Modelling and Grid Sensitivities

Gunther Wilke and Robin Gerlach
German Aerospace Center
DLR AS-HEL
Braunschweig, Germany

ABSTRACT

The prediction of the aerodynamic performance of the helicopter rotor at its operational boundaries is a challenging task. This study investigates the effect of various common numerical settings of computational fluid dynamic solvers onto the maximum thrust prediction of a hovering rotor. Thus, this study is distinguishing itself from other research as it leaves the usually analyzed regime around the maximum Figure of Merit. First, the impact of the time steps is investigated, coupled and followed by the spatial accuracy, the type of computational grid and lastly the impact of different turbulence models and their variations. It is observed that for moderate thrust around the maximum Figure of Merit of the rotor, the impact is little with respect to the difference at maximum thrust. The outcome is that the more recent adaptions of turbulence models should be applied in combination with a well resolved spatial resolution with a matching time step.

NOTATION

*

Symbols

$\Delta z/c_{ref}$ dimensionless background grid spacing in vertical direction

$\Delta\psi R/c_{ref}$ dimensionless background grid spacing in horizontal direction perpendicalr to the radial direction

ρ density of air

σ blade solidity

θ_0 collective pitch angle

A disc area

a_∞ speed of sound

c_nM^2 sectional normal force coefficient $c_nM^2 = 2dN/(\rho c(r) dra_\infty^2)$

c_tM^2 sectional tangential force coefficient $c_tM^2 = 2dT/(\rho c(r) dra_\infty^2)$

c_mM^2 sectional pitching moment coefficient $c_mM^2 = 2dM/(\rho c(r)^2 dra_\infty^2)$

$c(r)$ local chord length

c_T thrust coefficient $c_T = T/(\rho A v_{tip}^2)$

c_T/σ blade loading coefficient

c_P power coefficient $c_P = P/(\rho A v_{tip}^3)$

c_P/σ power loading coefficient

c_{ref} thrust weighted reference chord length

FM Figure of Merit $\frac{\sqrt{c_T^3}}{\sqrt{2}c_P}$

M_∞ flight Mach number

M_{tip} tip Mach number

Re_{tip} tip Reynolds number

r/R dimensionless radial position

v_{tip} tip speed

X/R dimensionless horizontal distance

Z/R dimensionless vertical distance

*

Acronyms

BDF Backward difference formula - applied for dual time stepping

DES Detached Eddy Simulations - blend of RANS and LES

ERF European Rotorcraft Forum

FT Fully turbulent - acronym of only used in this paper

LES Large Eddy Simulations - only structures smaller than the cell are modelled

LT Laminar turbulent transition prediction - acronym of only used in this paper

MUSCL Monotonic Upstream-centered Scheme for Conservation Laws

SA Spalart Allmaras turbulence model

SST Shear Stress Transport - here synomonous with Menter SST turbulence model

R Vortex/curvature correction in turbulence models

RANS Reynolds Average Navier-Stokes equations

VFS Vertical Flight Society

INTRODUCTION

The flow of a helicopter rotor is complex with many different phenomena present at the same time. For a forward flying helicopter, this will include shocks, dynamic stall and in general a very vortex dominated flow. In order to solve this, the inclusion of the blade dynamics is necessary, which due to their slender design are usually quiet flexible, or in cases of articulated rotors, flap. While hover is a less sever flight condition from this perspective, it is still remaining a very challenging flight condition as the wake and occurring tip vortices remain in the system for many revolutions of the rotor. In order to correctly model this, advanced computational fluid dynamics is necessary to do so. To this extend, it is still difficult to model the flight envelope of a helicopter independent of its flight velocity. McHugh (Ref. 1) tried to describe the lift and propulsive force limits trough wind tunnel experiments in 1978, and this research aims at finding this numerically for hover only.

In case of forward flight with the occurrence of dynamic stall posing the limit in maximum thrust, a good overview paper is given by Smith et al. (Ref. 2). They show where the current state of the art on experiments is, but also the do-ability in simulations. Regarding the latter, they state that for quasi 2D cases, large eddy simulations (LES) allow to correctly capture this phenomenon, but they are still prohibitively expensive in terms of computational cost. A reasonable alternative to LES are detached eddy simulations (DES), which at least on the qualitative scale allow for reasonable results. DES was envisaged by Spalart et al. (Ref. 3) for the SA turbulence model (Ref. 4) to be a bridge between Reynolds Averaged Navier-Stokes (RANS) simulations, and LES. The idea is to continue to model the small vortices of the boundary layer through eddy viscosity driven by the RANS turbulence model, and gradually transition to LES turbulence model away from the boundary layer. For helicopter flows, the delayed detached eddy simulations (DDES (Ref. 5)) become prominent as they ensure shielding the boundary layer to avoid premature stalling in case of insufficient resolution for LES near the wall, due model stress depletion. A good overview work on the application and shortcomings of DDES variants to rotorcraft problems including dynamic stall is given by Letzgus (Ref. 6) and Letzgus et al. (Ref. 7). They look into DSA-9A airfoil, but also the H145 helicopter. Another work showing the current possibilities to model the envelope of the rotor is given by Richez et al. (Ref. 8) for the UH-60A helicopter. Sridhar et al. (Ref. 9) look into the impact of using two different $k-\omega$ turbulence models onto simulation of the aero-elastic effects during dynamic stall of the 7A rotor.

Coming back to the hovering rotors, Chaderjian (Ref. 10) gives a good overview of his work around modelling hovering rotors with CFD and explains issues such as overproduction of eddy viscosity, the requirement to evolve the flow field for long enough to become meaningful and the occurrence of vortex worms. Latter have been seen in many simulations, but have really been experimentally proven by Wolf et al. (Ref. 11) and are now more formerly expressed as secondary vortices caused by the instabilities of the rotor wake and the primary tip vortices. Bodling et al. (Ref. 12) achieve a reasonable accuracy to model these instabilities to within the accuracy of the experiment. While this work already demonstrates the pinnacle of what can be done with CFD for rotors, reasonable guidelines on how to arrive there are not given. Lietzau et al. (Ref. 13) thus investigate the impact of varying spatial resolutions onto the accuracy of capturing just the primary tip vortex, but also analyze the two most popular turbulence models, namely the one equation SA turbulence model (Ref. 4) and the two equation ($k-\omega$) Menter SST (Ref. 14) model. They also include variations of these models that use either the vortex correction by Dacles-Mariani et al. (Ref. 15) or Shur et al. (Ref. 16). They both have been derived for the SA model and are then usually referred to as SA-R or SA-RC respectively. Other factors that influence the accuracy of hover predictions and most notable for the correct prediction of Figure of Merit is transition. A recent work utilizing intermittency transport models is given by Richez and Jain (Ref. 17) for dynamic stall cases. They find that with more simple semi-empirical transition models applied to turbulence models, the downstroke is reattaching too early, whereas the Langtry-Menter $\gamma-Re_\theta$ model requires a high spatial accuracy to capture the re-attachment process correctly in a dynamic stall cycle.

Coming back to the McHugh stall boundary, much work has been seen on dynamic stall in forward flight, which determines the maximum thrust. On practical level, often vibrations grow to large as to push the rotor into the lift stall of the complete rotor rather than a good portion of the middle sections of the blade on the retreating side. In hover, many investigations have been seen focusing on correctly predicting the Figure of Merit for a wide range of thrusts, but often these investigations are stopped roughly 1.2 times the thrust of the best Figure of Merit for a rotor. One of the reasons is that past this point, often no experimental data exists as either the wind tunnel motor cannot supply enough power past this point, or the experiment is stopped there due to too high levels of vibrations. In flight, this often also becomes the maximum the engines can supply to the rotor and the RPM will decrease past this point. Therefore, this study aims at finding the maximum thrust of what is aerodynamically possible, purposely leaving aside any interaction and elastic effects. The motivation to investigates this comes from van der Wall (Ref. 18) who exercised this with DLR's comprehensive code S4, who himself asked the question when seeing the rather wide spread of results after the STAR II prediction team activities (Ref. 19). Our studies were initially meant to complement his works, but were found to be too comprehensive by themselves already and therefore are presented here separately. They have been part of Gerlach's bachelor's thesis (Ref. 20).

Similar to Lietzau et al. (Ref. 13), but also Sridhar et al. (Ref. 9), and Chaderjian (Ref. 10), this study looks into the impact of spatial and temporal accuracy onto the performance prediction of the hovering rotor, but also different grid types and variations of the two common turbulence models, SA and SST. The distinguishing part from the previous studies is that the instead of the analyzed regime around centered around maximum Figure of Merit, the maximum thrust is sought being more complex and less researched for hovering rotors. The HART II rotor (Ref. 21) is used as the basis for the numerical tests, even though to isolate the aerodynamic effects, it is modelled as a fully rigid rotor without precone and in free stream.

METHODOLOGY

For this study, DLR's block structured legacy flow solver FLOWer (Ref. 22) is employed. Here, the inviscid SLAU2 (Ref. 23) is used with the Mach switch based on the interface normal instead of total velocity as proposed by Tanabe et al. (Ref. 24) for the rFlow3D code by JAXA. Similarly, the FCMT reconstruction by Yamamoto and Daiguiji (Ref. 25) is used, yet with the modification of using the van Albada limiter (Ref. 26) instead of the minmod limiter, which has shown to drastically improve accuracy and robustness, see (Ref. 27). For the temporal solution, either steady flow is assumed with pseudo-time steps being solved through the LU-SGS scheme by Yoon and Jameson (Ref. 28) or unsteady flow is modelling us-

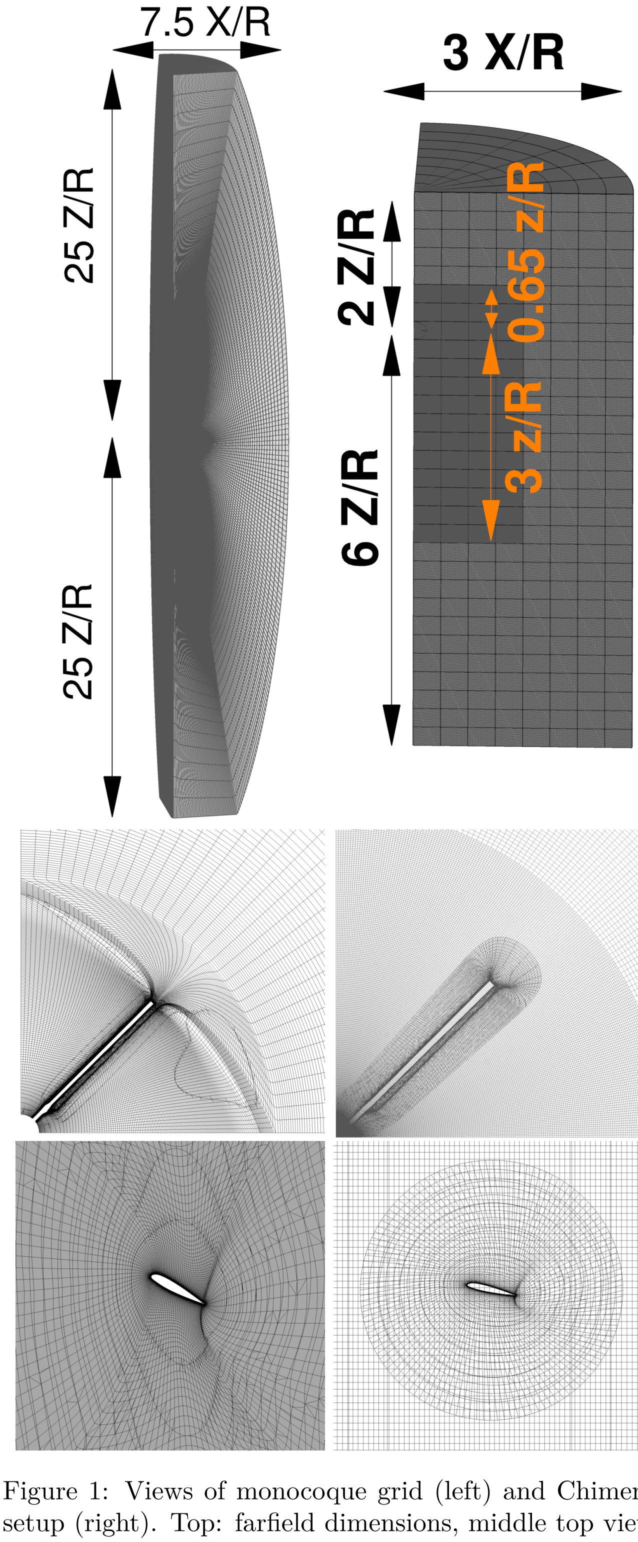

Figure 1: Views of monocoque grid (left) and Chimera setup (right). Top: farfield dimensions, middle top view slice of rotor plane, bottom side view of $r/R = 0.75$ slice.

ing the dual-time stepping approach with backward difference formulas (BDF). Here, the 1st, 2nd and 2nd+ order as proposed by Vatsa et al. (Ref. 29) are tried. Implicit residual smoothing by Swanson et al. (Ref. 30) is utilized for the acceleration of convergence. A pressure switch based reduction of the reconstruction order is also applied according to Radespiel and Kroll (Ref. 31) to ensure 1st order reconstruction near shocks. The here utilized turbulence models are the SA turbulence model (Ref. 32) and Menter SST model (Ref. 14). The SA model is also tried with the vortex correction by Dacles-Mariani et al. (Ref. 15) (SA-R), but also delayed detached eddy simulations (DDES) (Ref. 5). The SST model is also tried with a vortex correction (here also simple extended as SST-R) according to Dol et al. (Ref. 33). It was originally perceived for the Kok $k-\omega$ turbulence model (Ref. 34), but can also be applied to the SST model in FLOWer. The SST model is also tried with the DDES extension through the adoption of DES for $k-\omega$ turbulence models by Gritskevich et al. (Ref. 35). For the SA model, the turbulence model values have been reconstructed using a 2nd order MUSCL scheme, and have been computed at 1st order for the SST model while the same contravariant velocity from the main equations is used (hybrid order). Both turbulence models are also tested with empirical laminar-turbulent transition prediction according to Heister (Ref. 36), whom himself bundled known transition criteria to be used at the same time. This includes the prediction of Tollmien-Schlichting waves, C1 cross-flow, attachment line and bypass transition. Since the rotor is modelled in hover, the outer state of the farfield boundary condition is modified with the source/sink model and assuming wake contraction instead of assuming Mach number zero, also known as Froude boundary condition. An example is given in Beaumier et al. (Ref. 37). The viscous variant based on Spalart's jet theory (Ref. 32) as implemented by Jia et al. (Ref. 38) was concurrently implemented and tested in FLOWer, but did not find application here. The numerical part of farfield condition itself is based on Whitfield (Ref. 39). To handle overlapping grids, the Chimera approach is utilized implemented by Schwarz (Ref. 40) into the FLOWer code. The here used Lagrangian interpolation reaches up to 8th order on Cartesian grids, but deteriorates for increasing curvature of the grid lines.

An important part of these studies are the numerical grids, which have been generated with the in-house grid generator G-Cube, first mentioned in the appendix of Wilke (Ref. 41) and used in many recent rotorcraft studies. It follows many ideas of the GEROS grid generator by Allen (Ref. 42), most notably the transfinite grid interpolation. G-Cube allows to generate simple blade grids, background meshes of Cartesian, but also cylindrical type. Another specialty taken from GEROS are the monocoque grids for rotor and propellers in axial flights, which allows to compute hovering rotors without the utilization of Chimera/Overset. This trades the interpolation error of the Chimera boundary with the loss of accuracy of the spatial scheme due to skewed cells. In particular for (very) low cell counts, these grid types produce reasonably good results with respect to wind tunnel experiments as demonstrated in Wilke (Ref. 43). When more grid cells are available, the use of a Chimera setup becomes more viable due to the more regular cells in the background mesh as will be shown in the results section. In Figure 1, the two setups are sketched for comprehension. Both exploit the periodicity of the rotor and thus only model a quarter of the rotor. Thus, fully Cartesian grids are not considered here, but the cylindrical background grid is quadratic with respect to the vertical and radial axis. The according grid points of the blade surface grid, but also the overall grid are listed in Table 1.

Grid type	Monocoque	Chimera
chordwise	128	
radial	128	
BL[1]	≈ 30	
normal	128	64
$\Delta z/c_{ref}$	0.37	0.14
$\Delta\psi R/c_{ref}$	0.45	0.19
blade	2.1e6	1.0e6
background	0.7e6	2.1e7
total	2.8e6	2.2e7

Table 1: Respective grid numbers for used on the finest respective grid. [1] BL: boundary layer.

All setups were run until either the density residual dropped to 5e-5 of the initial residual (the very first subiteration of the simulation) or until 100 inner iterations have been reached for the unsteady simulations or 50,000 iterations for the steady simulations. With respect to the residual of the first inner iteration of the respective time step, this leads to roughly 1.5 order of magnitude drop in the final stages of the simulation. However, in the maximum thrust regime for the successively finer grids, only 0.75 magnitude drop could be achieved, or 1e-4 with respect to the very initial residual. All cases are run for at least 30 revolutions. The maximum number of revolutions has been estimated by $n_{rev} = \frac{Z/R}{\Pi\sqrt{c_T}}$ with Z/R set to 6 roughly corresponding to the distance required to consider the rotor out of ground. The equation is derived assuming how long the wake needs to reach this distance at which it is considered to have a negligible impact on the rotor thrust and torque. The estimate shows to be reasonable as the leveling off of thrust and torque around a mean value as envisaged by Chaderjian (Ref. 10) was seen.

The respective time steps, applied turbulence model and other settings are then explicitly mentioned in the results section.

RESULTS OVERVIEW

The selected rotor for this study is based on the HART II rotor (Ref. 21). The rotor parameters are summarized in Table 2. Since the focus lies on investigating the impact of different numerical parameters onto the solution of maximum thrust, it has been computed as a rigid rotor without precone. Only the collective pitch angle is altered to cover the thrust range from the maximum Figure of Merit to maximum thrust and slightly past it.

Table 2: Rotor parameters and baseline flight condition.

	HART-II
R	2 m
c_{ref}	0.121 m
twist	$-8^o/R$
airfoil	NACA 23012 with tab
M_{tip}	0.64
Re_{tip}	1.8e6
M_∞	0.0

The results are organized into four main sections: temporal accuracy, spatial accuracy, grid type, turbulence models and variations. The last study based on turbulence models is further split into three parts where first the SA model is investigated, then the SST model and lastly selected cases of both are compared with each other.

TEMPORAL ACCURACY STUDIES

In this study, the impact of the various possible temporal accuracy is investigated. This also includes steady simulations. Since the Navier-Stokes equations couple space and time, it is difficult to investigate the temporal accuracy completely decoupled from spatial accuracy. Therefore, a variation of space will also be included here. The formally 2nd order accurate MUSCL reconstruction has been applied and the plain SA turbulence model has been used. For simplicity, these studies have been carried out on the monocoque grids with 3.6e5 and 2.8e6 points. For the temporal side, the following variations are tried:

- steady - local time stepping is used to advance towards infinity
- BDF1 - 1st order dual time stepping with $\Delta\psi = 1^o$ time step equivalent
- BDF2 - 2nd order dual time stepping with $\Delta\psi = 1^o$ time step equivalent
- BDF2OPT - enhanced 2nd order dual time stepping with $\Delta\psi = 2^o$ time step equivalent
- BDF2OPT - enhanced 2nd order dual time stepping with $\Delta\psi = 1^o$ time step equivalent
- BDF2OPT - enhanced 2nd order dual time stepping with $\Delta\psi = 0.5^o$ time step equivalent

In Figure 2, the integral coefficients of the rotor are presented. For the steady simulations, the average of the last 500 iterations is taken, and for the unsteady simulation, the last revolution was averaged. The continuous lines present the study results, while the dashed lines present the unsteady results. For the lower collective pitch angles, a good agreement between the methods is observed for the thrust, yet for the required power as well as the Figure of Merit the steady results deviated noticeably. The temporal variation, no larger differences are observed on the coarse grid of 3.6e5 grid points. After further investigation of the flow field, it was found that the steady simulations feature very high levels of eddy viscosity, which are not found for the unsteady simulations. Looking at the result for the finer grid, it is observed that the stall behavior has changed again remarkably with respect to the other studies. Where the maximum Figure of Merit is almost the same for the coarse and fine grid, the stall behavior shows a large difference.

To gain further insights into the resolved physics, the averaged sectional loads of the rotor are plotted for the pitch angles $10, 24, 28^o$, roughly corresponding to the settings for maximum Figure of Merit, maximum thrust and post rotor stall. When looking at the normal force at 10^o pitch, the steady simulations show a little of the overshoot from the incoming tip vortex, which has been diffused by eddy viscosity. For the other simulations, the trend is very similar, with a mildly more pronounced impact of the preceding vortex for the higher resolved grid. This is even better visible when looking at the tangential sectional force and even the pitching moment. Moving onto the maximum thrust angle of 24^o pitch, a match of all methods on the inboard station is found up to roughly $r/R = 0.6$, but past this point a large spread is found. The steady results show a different behavior, with the finer grid results leaning more towards the unsteady results. The unsteady results on the coarse grid are close to each other, with the unsteady result on the finer grid showing a further reduction of thrust towards the tip. For the tangential loads, the steady results already show a larger drag on the inboard stations caused by the high levels of eddy viscosity, whereas the unsteady results align up to roughly $r/R = 0.5$, with the unsteady results for the finer grid showing a greater reduction then the coarse grid results. A similar trend for the pitching moment is observed, yet for the finer grid the oscillation of the pitching moment becomes even larger than for the coarse grids, with the steady results in between. For the post stall angle, the steady simulations still show no sign of a strong separation attributed to the damping effect of the high eddy viscosity levels, yet interestingly, the coarse and fine grid results move closer together as in the previous case. At 28^o pitch, only small changes with respect to

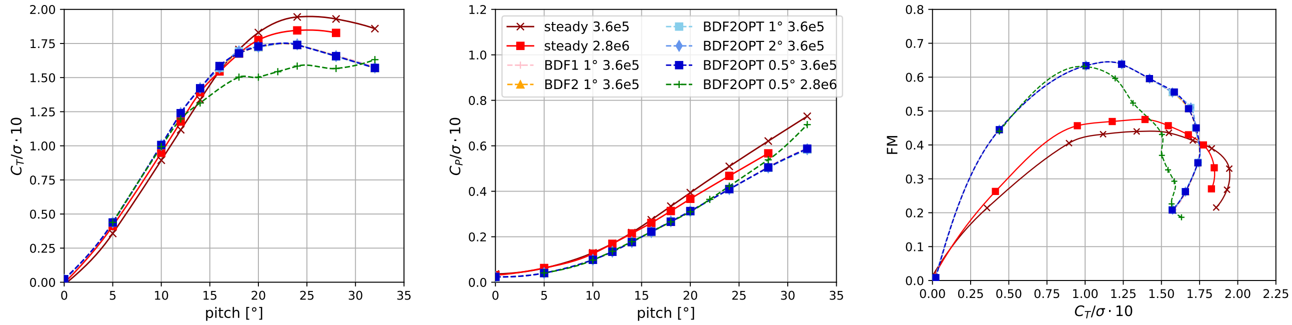

Figure 2: Averaged integral values of temporal accuracy study

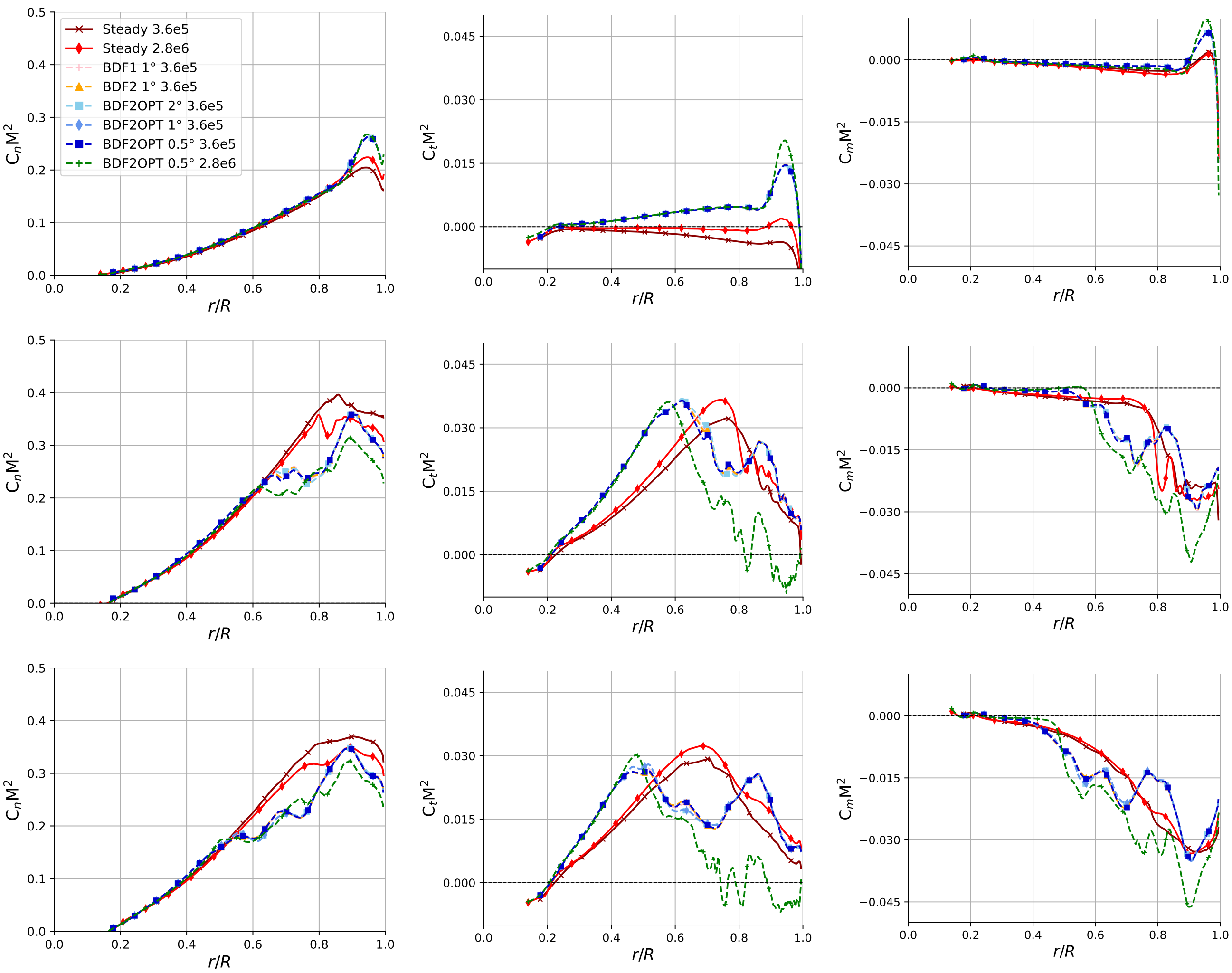

Figure 3: Sectional forces and moments at $\theta_0 = 10, 24, 28^\circ$ of temporal accuracy study

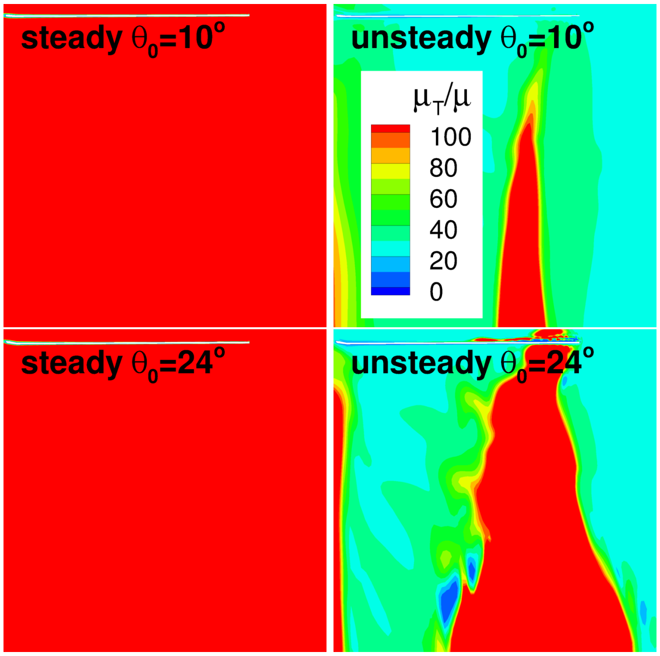

Figure 4: Eddy viscosity ratio for selected cases of temporal accuracy study. Left steady, right unsteady (BDF2OPT $\Delta\psi = 0.5^o$) simulation on 2.8e6 grid.

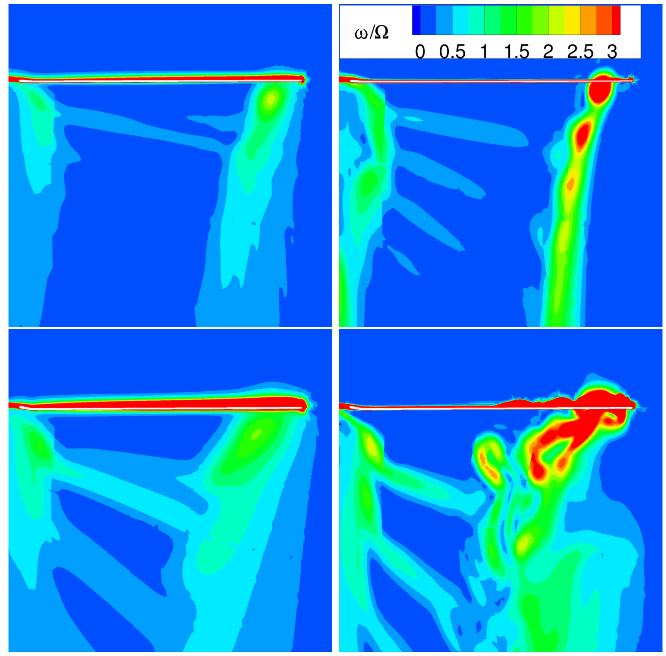

Figure 5: Vorticity ratio for selected cases of temporal accuracy study. Left steady, right unsteady (BDF2OPT $\Delta\psi = 0.5^o$) simulation on 2.8e6 grid.

the previous angle are observed in terms of features, even though in the individual wiggles are differently aligned.

As an intermediate summary of the temporal studies, it is noted that the SA turbulence model and steady hover simulations may lead to overly high levels of eddy viscosity that tend to diffuse the tip vortices too much and alter the results strongly. This is something that Chaderjian (Ref. 10) also observed for unsteady simulations. This is additionally elaborated in Figure 4 and Figure 5. The eddy viscosity levels become very high for the steady simulations, but remain within reasonable levels for the unsteady simulations. The reason for this is that the SA turbulence model loses its destruction term far off from the wall, and therefore the production term triggered also by vorticity starts to gradually flood the flow field. It is believed that given enough revolutions, the flow field will also flood with eddy viscosity for unsteady simulations. Also, from these pictures it is observed that a higher thrust will lead to more production of eddy viscosity also being triggered from the separation vortices and not only the tip vortices themselves. A potentially remedy to this eddy viscosity flooding of the SA model is proposed by Hong et al. (Ref. 44), but shall not be topic of this paper as it was concurrently developed with these results.. With respect to the temporal required accuracy, the impact of various settings was little, but from the added spatial variation it may be concluded that a specific time step should be tied to a specific resolution of the grid. From a practical perspective, reducing the number of time steps simply led to an increase of inner iterations to reach the same stopping residual, thus the impact on cost was little, and therefore it was decided to stay with the BDF2OPT scheme and 0.5^o for the finer grid, and 1.0^o for the coarse grid.

SPATIAL ACCURACY STUDIES

For the spatial accuracy study, the formal order of the inviscid flux scheme is varied between 2 and 4, while also the grid density is varied between 3.6e5 and 2.8e6 cells. Otherwise, the style of presenting the results remains the same, first the integral results in Figure 6 and sectional loads in Figure 7. Due to the coupling of time and space of the Navier-Stokes equations, as previously mentioned, steady and unsteady results are presented. The unsteady results all utilized the BDF2OPT dual time stepping, with $\Delta\psi = 1^o$ and $\Delta\psi = 0.5^o$ for the coarse grid 3.6e5 and fine 2.8e6 grid.

Looking at the integral results in Figure 6, the greater maximum thrust for the steady simulations is again observed similarly to the previous study, with the unsteady simulations showing a faster, but more flat stall. Again, the reason lies in the occurring eddy viscosity flooding of the flow field for the steady simulations, which stabilize the flow at the cost of increased drag. The impact of the spatial accuracy appears to be secondary to this issue, nevertheless, it is observed that a higher spatial accuracy, be it grid points or formal order of the inviscid scheme, lead to reduced torque before the point of maximum Figure of Merit, but an increase past it. For this specific grid type, where no regular cells can be achieved, the utilization of more grid points has a stronger impact than the application of higher order schemes. Around the thrust plateau for the higher resolved unsteady simulations, the 4th order results show slightly reduced thrust

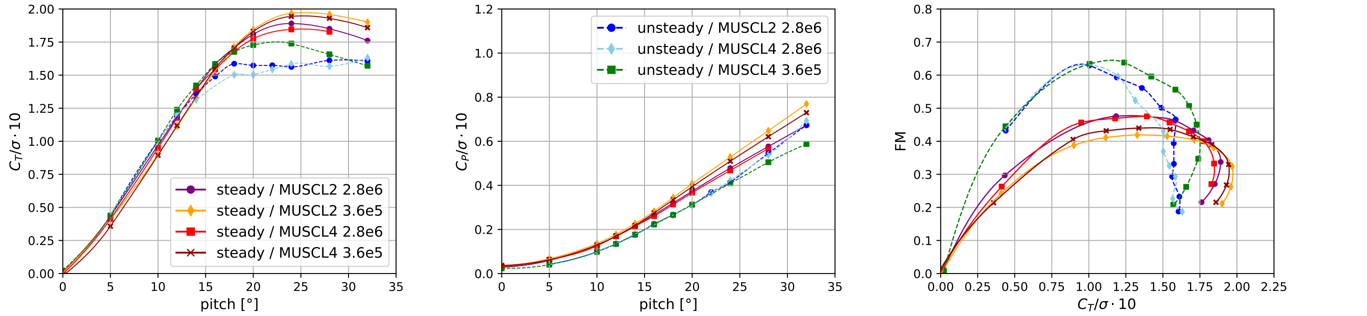

Figure 6: Averaged integral values of spatial accuracy study

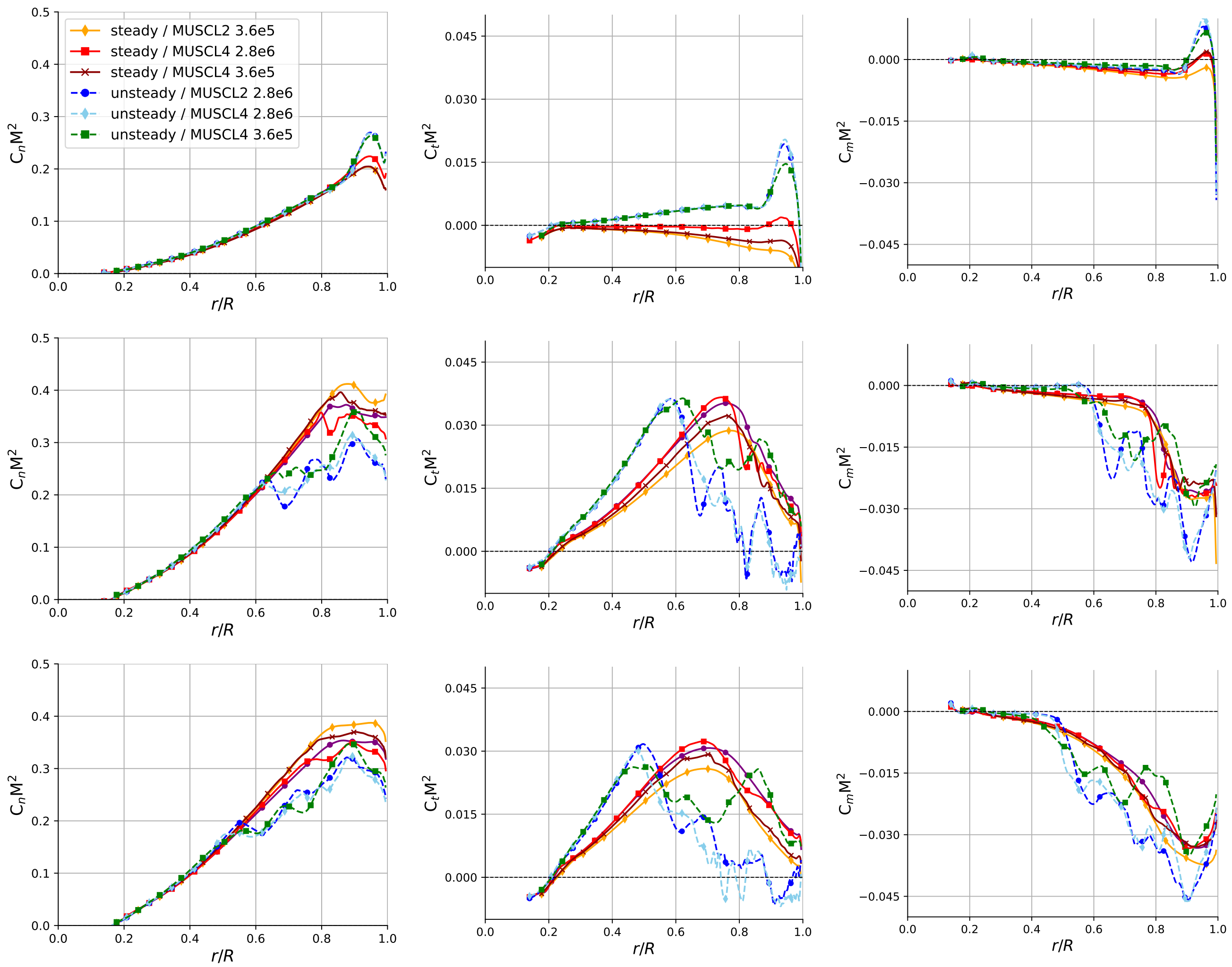

Figure 7: Averaged sectional forces and moments at $\theta_0 = 10, 24, 28^\circ$ of spatial accuracy study

with an increase in torque, hence a reduced Figure of Merit in this regime. The coarse grid unsteady results lean more towards the steady results, with the reason being the coarse resolution is synonymous with artificial dissipation and therefore has a similar impact as the increased eddy viscosity of the steady simulations.

The sectional loads (Figure 7) show again the trend that the steady simulations do not resolve the previous tip vortex well and only the unsteady simulations show the lift overshoot in the normal force coefficient at $r/R = 0.95$ at 10^o pitch. The tangential force shows a more pronounce behavior here for the finer grids, but generally all unsteady simulations are quite close to each other. Again, the lower resolved unsteady results show a tendency towards the steady results with the eddy viscosity flooding, yet arises from the under resolution rather than the overproduction of eddy viscosity. At the 24^o pitch, which is roughly the maximum thrust for steady simulations, the steady simulations show a fairly high normal force with an onset of lift stall around $r/R = 0.8$, while the unsteady simulations show stall behavior starting around $r/R = 0.6$. The tangential force is also split here, where the unsteady simulations show a greater reduction due to the separation with the exception of the coarse grid result. The pitching moment stall behavior is coupled with the normal force stall and the unsteady section show signs of stall beginning at $r/R = 0.6$ and the steady results at $r/R = 0.8$. For the post stall angle of 28^o, the steady simulations still show a very benign behavior, whereas the unsteady results are fairly aligned, and the coarse grid normal force is close to the finer grid ones, while the tangential force and pitching moment are further away. The pitching moment of the steady simulations appear like a smoothed variant of the unsteady simulations with its magnitude in a similar range.

The intermediate summary of the spatial accuracy study revealed that the utilization of more grid points is more beneficial than the application of higher order schemes. In Figure 8, the eddy viscosity and vorticiy plots for the finer grid at 4th order, please compare with Figure 4 and Figure 5. This shows that the application of the higher order scheme enhances the flow field as roughly one vortex passage more is preserved in contrast to the 2nd order solution. Since the cost for running the 4th order scheme only reveals that the increase in runtime is roughly corresponding to the increase in accuracy. Thus, the successive studies are carried out at 4th order. As will be seen in the next sections, the here applied scheme benefits from being applied on a regularly space grid as the metric is still at 2nd order. Again, the application of steady simulations is found to be rather questionable, particularly for the thrust regime around stall and in combination with the plain SA model.

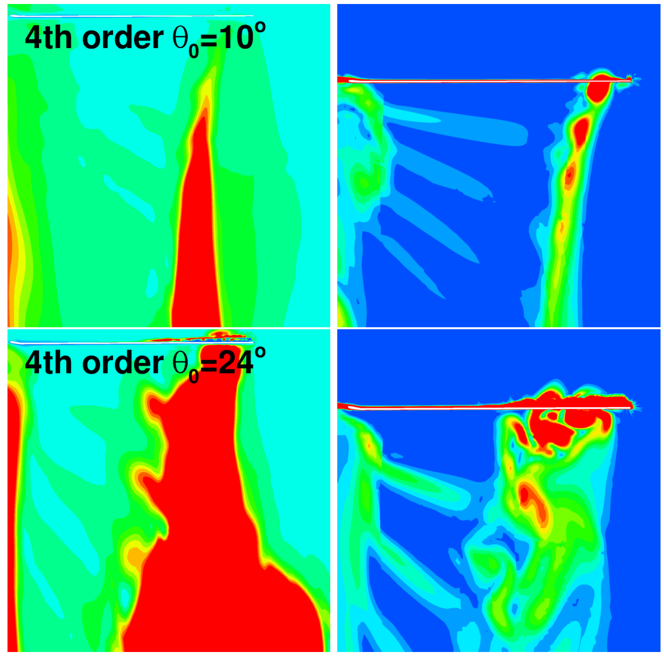

Figure 8: Left eddy viscosity ratio and right vorticity ratio plots for $\theta_0 = 10, 24°$ for the 4th order unsteady case using 2.8e6 grid points.

GRID TYPE EFFECT

This section will cover the effect of using a Chimera/Overset grid setup consisting of a background grid and a separate blade grid versus the utilization of a single, monocoque, grid. The advantage of the split grid approach is that the background grid can be made with more uniform cells, but an interpolation region between the two grids is required, which inherently will bring an interpolation error. Opposing this, the monocoque grid has no interpolation area, but to achieve a connected grid at the periodic boundaries, the cells need to be skewed which can only be mitigated to a certain extend. While the formal order of the here applied inviscid scheme is 4, the utilized metrics are of simple 2nd order. By simple, it is meant that it only strictly achieves 2nd order accuracy on Cartesian grids, but when cells are stretched, for example for boundary layers, the volume jump is neglected and therefore one should avoid how stretching ratios during the grid generation process to stay as close as possible to this 2nd order accuracy.

In order to achieve a good overlap for the Chimera/Overset approach, a minimum number of cells is required and therefore the coarser grid setup already has more grid points than the finer grid of the monocoque approach. For all grids, the 4th order MUSCL reconstruction is used in combination with the BDF2OPT scheme and the plain SA turbulence model. The integral coefficients are plotted in Figure 9. Interestingly, the results are juxtaposed. The fine grid Chimera results aligns well with the coarse grid monocoque results, and the coarse grid Chimera results

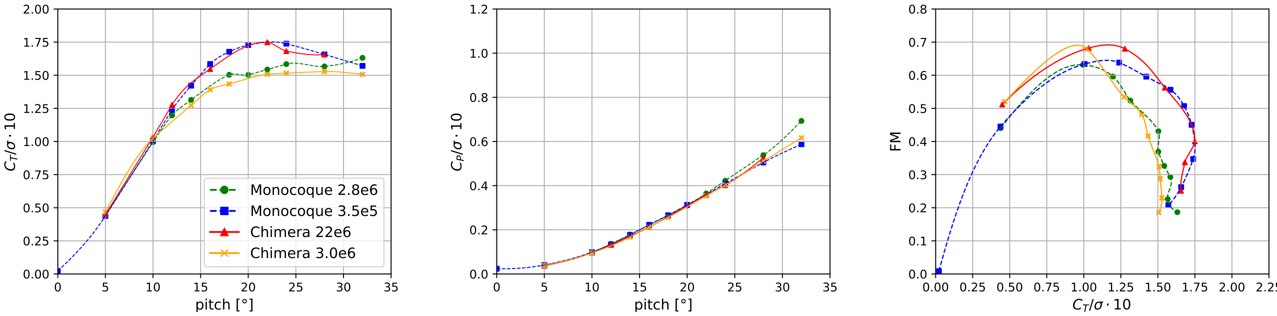

Figure 9: Averged integral values of grid type study

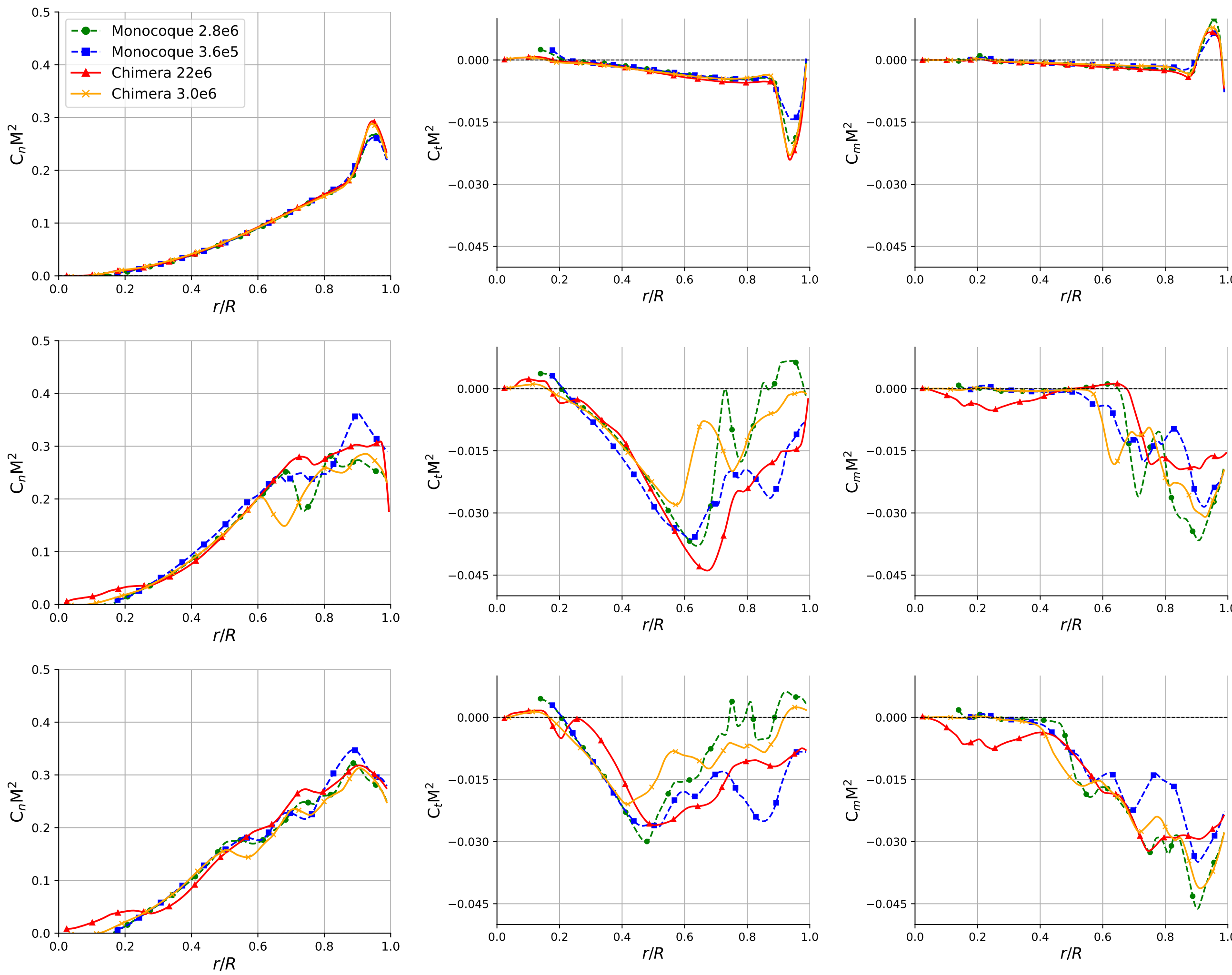

Figure 10: Averaged sectional forces and moments at $\theta_0 = 10, 22, 28^\circ$ of grid type study

aligns with the fine grid monocoque results. While for the lower pitch and thrust settings, the results don't deviate too much, the maximum thrust is different among the grids. However, no eddy viscosity flooding has been observed for the fine grid Chimera setup and thus seems to be valid in itself.

Moving onto the sectional forces in Figure 10, the sectional loads are plotted for the grid type study. At 10^o pitch angle, the normal forces align up to $r/R = 0.9$ and the overshot at $r/R = 0.95$ from the preceding vortex is simulated stronger with the Chimera grids. Looking at the tangential force, this trend is similarly captured, yet the finer monocoque grid approaches the Chimera results. The pitching moment turns out to be fairly similar among the methods with the largest deviations again at the blade tip. For the pitch angle of 22^o degrees, the results are mixed like the integral values in this region. The actual outlier is the coarse monocoque setup, which shows already stalling section starting at $r/R = 0.6$, but has a normal force overshoot at $r/R = 0.95$. For the fine Chimera grid, the inboard sections also show signs of disturbed flow already, which the other grids do not resolve as such. For the post stall pitch angle of 28^o, the normal forces almost align again for all methods, yet the tangential forces are at different levels even though showing a similar waviness. The pitching moment is a bit more aligned among the grids, yet the coarse monocoque grid shows the strongest deviation at $r/R = 0.8$.

This study shows that the grid type also has a noticeable role on the maximum lift prediction. Yet, it cannot be concluded which one is more suited simply looking at the results. However, in combination with the spatial accuracy study, it is believed that the better resolution of the finer Chimera grid, but also the more regular background grid will yield better results and therefore the next study will be conducted with the fine Chimera grid.

IMPACT OF TURBULENCE MODELING

So far, the studies have utilized the SA turbulence model. Yet looking at the papers presented at the 80th Vertical Flight Society Forum and the 50th European Rotorcraft Forum from the year 2024, roughly one third of the papers utilized the SST turbulence model and roughly half of the papers utilized the DES modification for either turbulence model. Thus, this section more deeply investigates the impact of adding popular modifications to the SA and SST turbulence model, but also include laminar-turbulent transition prediction to study the impact on the maximum thrust.

SA Variations

The SA turbulence model is one of the two major turbulence models currently applied for rotorcraft applications. Spalart himself proposed the idea of detached eddy simulations (DES) (Ref. 3), a hybrid of the classical RANS approach, which attempts to model every vortex through turbulent viscosity, and Large Eddy Simulations (LES), where only vortices smaller than the grid cell size are modelled through turbulent viscosity. DES thus attempts to merge both approaches, where the attached boundary layer is modelled by RANS, but larger scale vortices as occurring during separation are treated by LES. This modification also lends itself quite nicely for rotorcraft flows, because they are vortex dominated, but those primary tip vortices are several orders of magnitude larger than the boundary layer. Here, the delayed detached eddy simulation (Ref. 5) is utilized. Another modification of the SA model has been proposed by Dacles-Mariani et al. (Ref. 15), who reduce the production term of the SA model, if the strength of vorticity exceeds the strength of the shear tensor. The idea is that in these cases, a free vortex is given and no production of eddy viscosity is required in its core. In practical terms, the DES modification fosters the destruction term in the field of the SA model, which otherwise would become diminishing small as it is inversely proportional to the distance of the nearest wall. This modification is usually denoted R or recently also as R95. Both modifications are tried here individually, but also in combination. Most of them are run on the coarser Chimera grid for reduced computational cost, but the all-inclusive variants are also tried on the finer mesh. They are tried fully turbulent (FT) and with laminar turbulent transition prediction (LT).

The integral values of the SA study are presented in Figure 11. The plain SA model shows a high maximum thrust, but the lowest Figure of Merit, which is attributed to eddy viscosity flooding. It is less severe than for the monocoque grids, but still eminent. The R modification seems to mostly remedy this already for this grid. The DDES extension shows an even stronger drop in maximum thrust on the coarse grid, with the combination of DDES-R showing the least maximum thrust with a similar high maximum Figure of Merit as the DDES only modification. The inclusion of the laminar-turbulent transition prediction increases maximum thrust and maximum Figure of Merit. Increasing the grid density also raises the maximum thrust and Figure of Merit again, with the laminar-turbulent transition prediction achieving the highest values.

Moving onto the sectional loads shown in Figure 12, the normal forces for the 10^o pitch are close to each other with a larger spread in the tangential forces with the plain SA model on the coarse grid showing the greatest difference to the other variants at the blade tip. The pitching moment is very similar for the variants with the exception of the plain SA simulation on the coarse grid. For the 22^o scenario, the normal force coefficients show signs of stall at $r/R = 0.7$ for the plain SA model variant, but also the R variant having the greatest peaks at $r/R = 0.85$. For the tangential loads and the pitching moment,

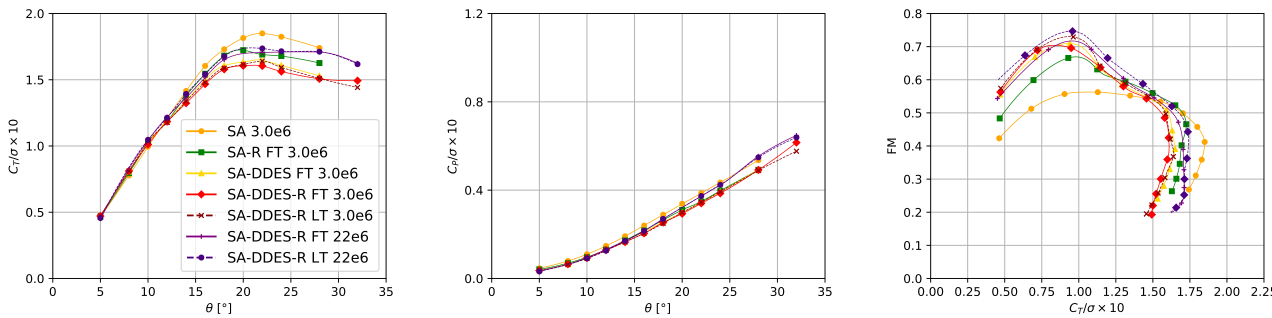

Figure 11: Averaged integral values of SA variants study

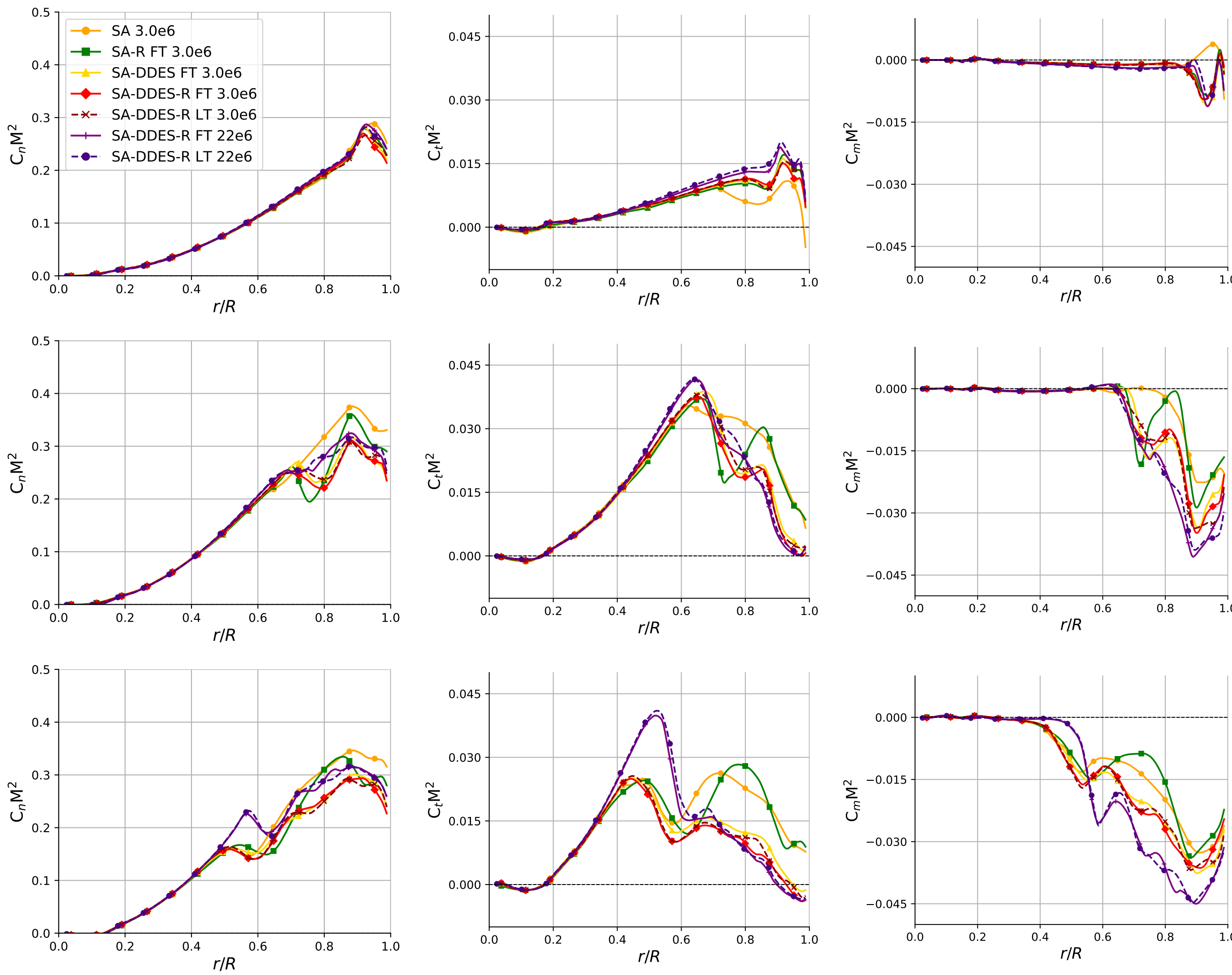

Figure 12: Averaged sectional forces and moments at $\theta_0 = 10, 22, 28°$ of SA variants study

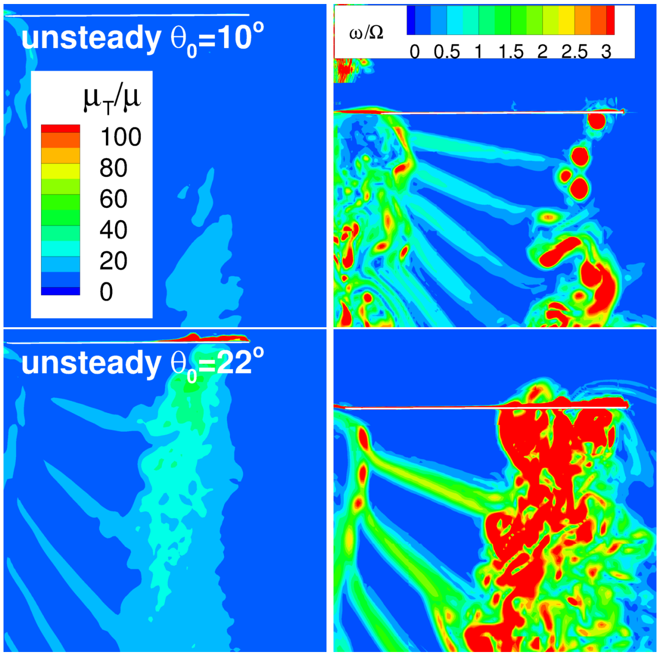

Figure 13: Left eddy viscosity ratio and right vorticity ratio plots for $\theta_0 = 10, 22^\circ$ for the SA-DDES-R LT case using 22e6 grid points.

a chaotic spread is observed. For the pitching moment, the finer grid results distinguish themselves by having the greatest negative peak. This trend also persists for the post stall angle of 28^o. The coarse grid results are now relatively close to each other for the normal and tangential forces, with the finer grid results showing a distinct peak at $r/R = 0.55$.

For the SA study, employing the DDES and R modification already improve on the eddy viscosity flooding effect of the plain SA model. The combination of both reduces the injected eddy viscosity. The impact of the grid density is on a similar scale as either modification. The inclusion of laminar-turbulent transition prediction mostly unfolds before maximum Figure of Merit mostly regarding itself, but has little impact onto the maximum thrust. Investigating the transition lines, the suction side of the stalled sections are flagged as fully turbulent and therefore the high lift behavior is not altered too much over the fully turbulent simulation. In the non-stalled areas, the laminar flow areas lead to a reduction of drag and hence torque. Elaborating a bit on the DDES extension, it is observed that the finer grid has noticeably less eddy viscosity than the coarse grid. The reason for this is that the DDES switch towards the LES simulation is triggered earlier due to the smaller cells in the field, but these smaller cells also lead to a reduction in injected eddy viscosity due to the reduction of filtering width associated with the characteristic cell size. Exemplary, for the finer grid and the SA-DDES-R LT simulations, the eddy viscosity ratio and vorticity ratio are plotted in Figure 13. In contrast to Figure 4 and Figure 5, it is observed that the application of eddy viscosity is drastically reduced and the vortex preservation is strongly improved, in particular for the subsequent vortex passages. The meandering known for these vortices is also now captured, which on the coarser monocoque grid is not possible due to the more dampened vorticity and higher eddy viscosity. Nevertheless, the turbulence model remains active and for the higher thrust setting, the injected eddy viscosity increases mimicking the higher frequent, smaller scale vortices, namely eddies, through eddy viscosity.

SST Variations

The SST model features a production limiter for both variables based on the destruction term. Thus, no eddy viscosity flooding as such has been observed as for the SA model, however, this clipping of values in combination with a difficult boundary condition for the destruction variable near the wall, leads to slower convergence than the SA model. Thus, the SST simulations required roughly 30% greater computational cost than their SA counterparts on average. Gritskevich et al. (Ref. 35) adopt Spalart's proposal of DES for two equation $k-\omega$ based turbulence models. The here denoted R modification alters the ω-Production term through multiplication of the maximum of the squared strain rate invariant and the squared vorticity. It has been described by Dol et al. (Ref. 33) for the Kok turbulence model, but is applied here for the Menter SST turbulence model.

The integral values are plotted in Figure 14 with the sectional loads presented in Figure 15. Here, the spread between the variations is less than for the SA variants. The addition of R and DDES both reduce the maximum thrust as observed for the SA model, but the drop is less pronounced. The inclusion of laminar turbulent flow mildly increases the maximum thrust and Figure of Merit. Regarding the sectional loads, for the collective pitch angle of 10^o, the non-DES results show a different location of the normal force peak than the SA model being at $r/R = 0.9$ instead of $r/R = 0.95$ as found for the SST-DDES variants, but also all SA models. This is also replicated by the pitching moment. Only a mild deviation in the tangential force is found between the methods. At the stall angle of 24^o, the SST variations split into two groups. The SST and SST-R variant show a later stall behavior with sections stalling past $r/R = 0.7$, whereas the DDES based variants start to stall at $r/R = 0.6$. For the post stall angle of 28^o, the SST-R now aligns with the DDES results, and the plain SST variant shows a slightly different behavior.

For the SST investigation, the brief summary is that the results are less spread over the variations, nevertheless, it seems that the DDES extension as the largest impact and seems to align results closer to the SA(-DDES) model results.

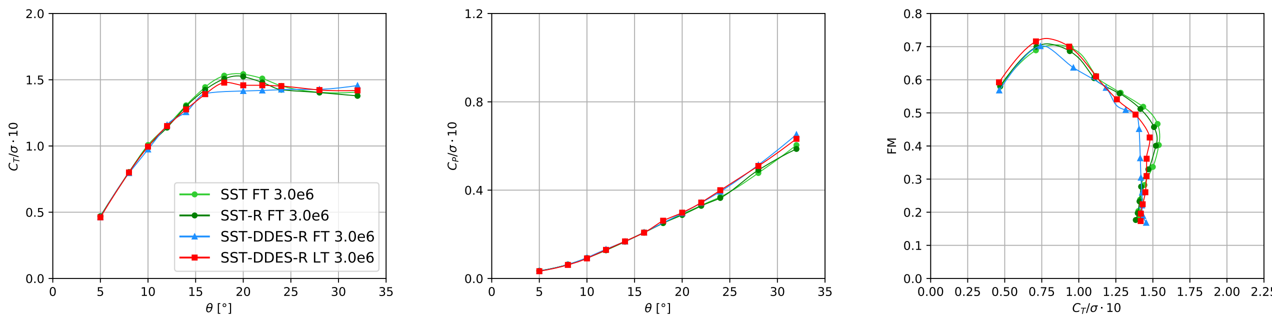

Figure 14: Average integral values of SST variants study

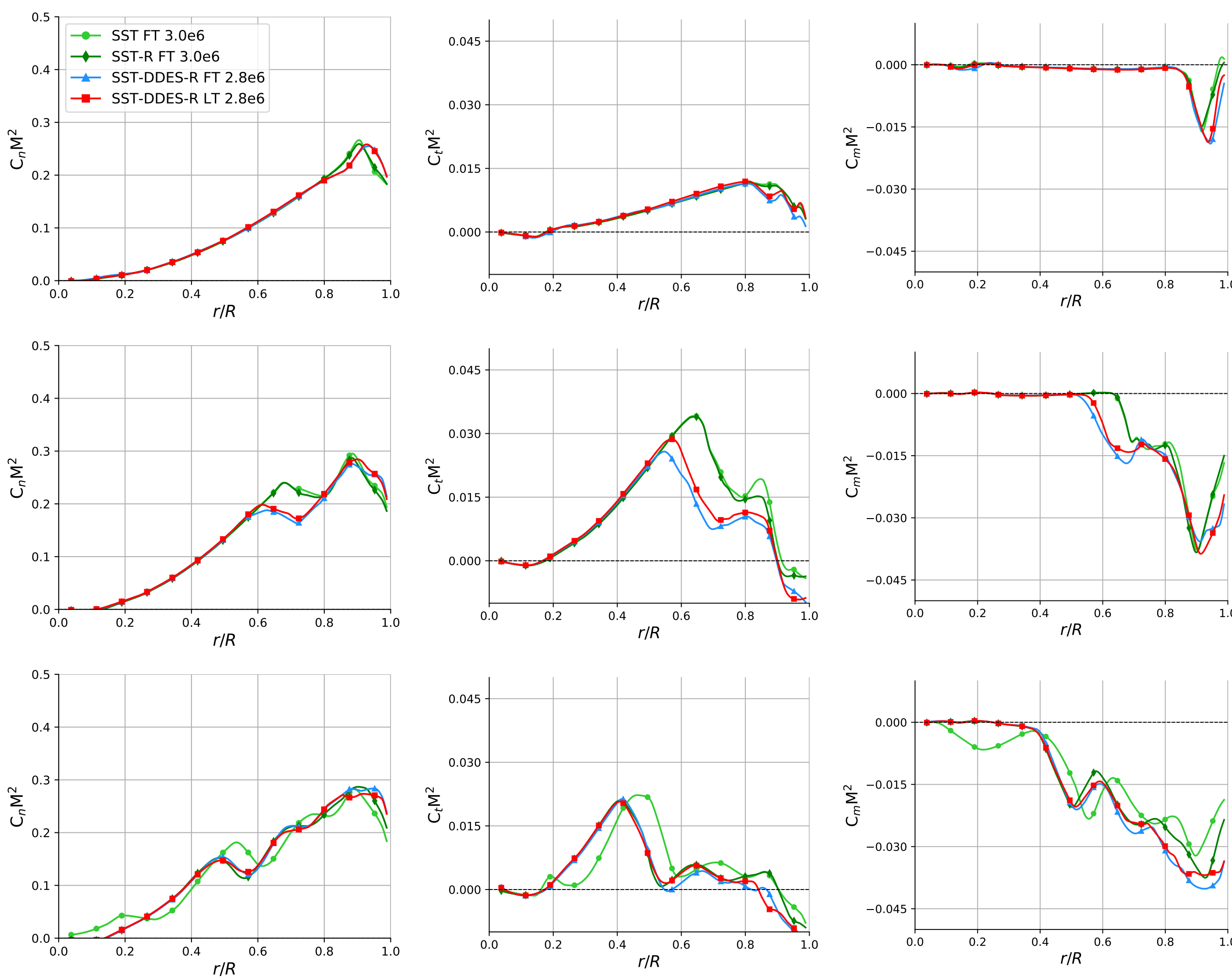

Figure 15: Averaged sectional forces and moments at $\theta_0 = 10, 22, 28^\circ$ of SST variants study

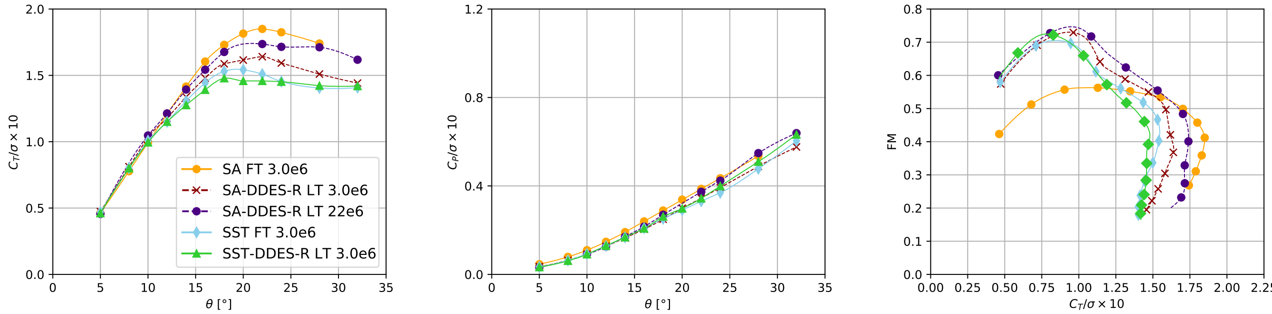

Figure 16: Averaged integral values of comparison of SA and SST turbulence models

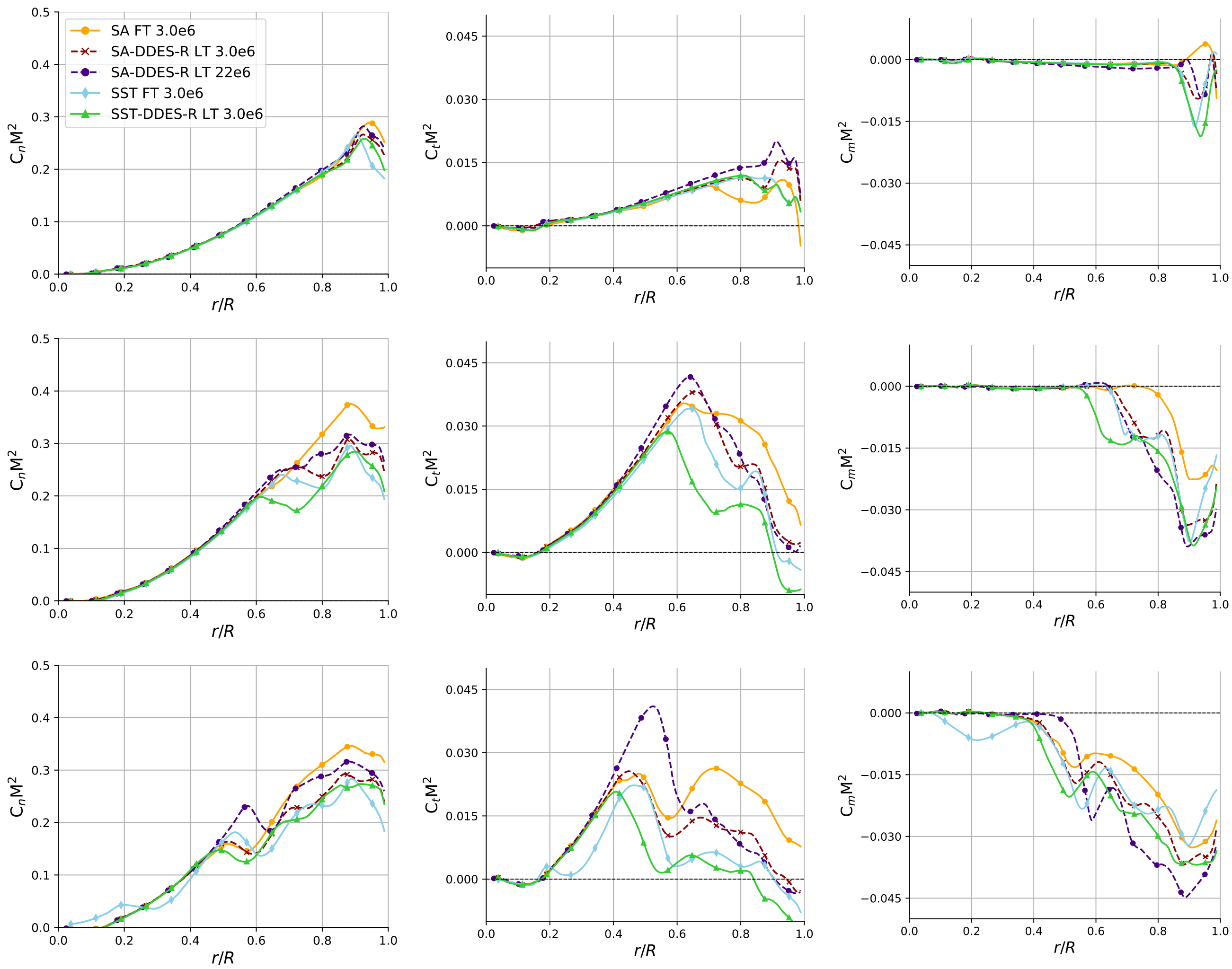

Figure 17: Averaged sectional forces and moments at $\theta_0 = 10, 22, 28^{\circ}$ of comparison of SA and SST turbulence models

Comparison of SA and SST

In this section, no new results are presented, but simply a selection of SA (dashed lines) and SST (continuous lines) results are contrasted against each other. The plain models are shown, but also the fully extended version, DDES-R LT are presented for the coarse Chimera grid. Additionally, the fine Chimera grid result for the SA-DDES-R LT model is shown.

The integral values are plotted in Figure 16 and the sectional loads in Figure 17. From these plots it is seen that the baseline turbulence models themselves have a larger deviation than the DDES enhanced variants. For the inboard loads, the differences between the turbulence models are generally small, but the largest impact is seen near the tip where the tip vortex of the previous blade passes the blade. Here, the amount of eddy viscosity generated, but also the interaction with the boundary layer, shows that the turbulence model plays crucial role. Thus, the SST results feature lower maximum thrust and Figure of Merit values than their respective SA counterparts. The fine grid SA-DDES-R LT result actually delivers a result in-between the spread of coarse grid SA and SST results.

While further studies would be required, the normal force results at 10^o pitch indicates that potentially with the DDES-R extension, the SA and SST result move closer to each, at least for non-separated flow. In combination with a finer grid it, where more of the flow is modelled as LES instead of RANS and hence the impact of the baseline turbulence model is reduced, it is believed that results will align closer to each other. However, it is seen as long as these conditions are not given, the turbulence model play a crucial role in the prediction of maximum thrust of the rotor with a similar impact as resolution itself.

CONCLUSIONS

The HART II rotor blade has been modelled in a rigid fashion during hover flight seeking maximum thrust of the rotor. The numerical grids have been altered along with various but common solver settings. These include time step studies, investigation of the order of the inviscid scheme, two turbulence models and transition prediction. Key findings are that:

- It is imperative to run unsteady simulations to capture the maximum thrust correctly. However, the temporal resolution itself can be relatively low in the order of $\Delta\psi \approx 1$ and should be chosen such that the computational cost is minimized. E.g. too large time steps will be more difficult to converge, whereas too small-time steps will simply lead to too many computational cycles. On a pragmatic scale, the time step should become smaller with a finer grid to keep similar convergence behavior within the time step.
- The monocoque setup allows for an efficient setup, however, for increased accuracy, the Chimera approach becomes more viable with more grid points due to overall improved grid quality allowing to better maintain the formal order of the inviscid scheme.
- Spatial resolution is critical and may be achieved with a combination of high grid density and higher order inviscid schemes. Doubling the grid point in each spatial direction yielded a greater improvement than doubling the formal order of the inviscid scheme.
- The Spalart-Allmaras model may produce too much eddy viscosity by itself in hover, and the application of the DDES and R extensions is recommended as it mitigates the problem.
- The Menter SST model does not show this issue, yet, it was observed that converging the SST model is more costly than the SA model particularly for stalled conditions. The DDES and R extensions had less of an impact, but are still recommended to be used.
- For both, SA and SST turbulence models, the DDES and R extensions should be applied as they reduced unnecessary eddy viscosity and model the primary vortices better and eventually allow to capture the secondary vortices, which otherwise would be smeared out by too much eddy viscosity.
- The inclusion of laminar-turbulent transition prediction has a minimal impact on the maximum thrust prediction as stalled section are fully turbulent on the suction side.
- Independently of the applied numerical setup, the stall angle for the rotor was in between $20-24^o$ collective pitch. The blade loading varied between $c_T/\sigma \approx 0.140.19$. The first stalling sections were found at the blade tip, where the tip vortex of the previous blade led to a too high angle of attack and the sections stalling. This grew inboard to roughly $r/R = 0.6$ for the maximum thrust of the rotor. The stall curves are of parabolic to flat nature. For better resolved simulations, the flatness is greater than for lower resolved simulations. Some oscillations around the maximum thrust are observed for the thrust curves on the finer grids, likely associated with the general unsteady nature of the problem at hand and an averaging of more than one revolution

No statement on the correctness of either SA or SST can be made here. This study aimed at simply showing the impact of various settings to the flow solver, seemingly available in most codes applied to rotorcraft. However, from a logical perspective, the impact of the underlying baseline turbulence model should become smaller when DDES is applied as less and less is modelled through the turbulence model and more and more is resolved through the solution of the Navier-Stokes equations with increasing resolution, which hinge on Newton's principles. Therefore, a clear recommendation is given for the utilization of DDES for rotorcraft applications. While the gray area of those approaches are still part of ongoing research, on a practical scale, issues around it can be resolved by modifying coefficients of the switching functions, as Letzgus (Ref. 6) or Chaderjian (Ref. 10), among others, show. Even on coarse grids they seem to improve results, and while Spalart (Ref. 45) warns in his DES guide that results may become more correct for the false reasons, it still seems to be a viable option to arrive at better results. However, the author's would refrain from simply disabling the turbulence model altogether in the background grid as Yoon et al. (Ref. 46) did. Despite the improved results, the higher frequent, potentially tertiary vortices, are better off being modelled than resolved.

For future research it is recommend to use a stronger solver to increase the fidelity of solving the set equations, even finer grids and time steps, but also looking into the impact of resolving the secondary vortices when impinging on other components of the rotorcraft. The underlying question here is, whether it is necessary to resolve these secondary vortex structures for design decisions, or if existing turbulence models could be modified to correctly mimic the behavior for design decisions from less resolved and cheaper simulations.

AKNOWLEDGEMENTS

The authors gratefully acknowledge the scientific support and HPC resources provided by the German Aerospace Center (DLR). The HPC system CARA is partially funded by "Saxon State Ministry for Economic Affairs, Labour and Transport" and "Federal Ministry for Economic Affairs and Climate Action".

CLASSIFICATION & COPYRIGHT

REFERENCES

1. F. J. McHugh, "What are the Lift and Propuslive Force Limits at High Speed for the Conventional Rotor," 34th Annual National Forum of the American Helicopter Society, 1978.

2. M. J. Smith, A. D. Gardner, R. Jain, D. Peters, and F. Richez, "Rotating Wing Dynamic Stall: State of the Art and Future Directions," 76th Annual Forum of the Vertical Flight Society, 2020. DOI: 10.4050/F-0076-2020-16472.

3. P. Spalart, and W.-H. Jou, M. Strelets, and S. Allmaras, "Comments on the feasibility of LES for winds, and on a hybrid RANS/LES approach," Vol. 1, May 1997, pp. 4–8.

4. S. Allmaras, F. T. Johnson, and P. Spalart, "Modifications and clarifications for the implementation of the Spalart-Allmaras turbulence model," Seventh International Conference on Computational Fluid Dynamics (ICCFD7), January 2012.

5. P. R. Spalart, S. Deck, M. Shur, K. D. Squires, M. Kh. Strelets, and A. Travin, "A New Version of Detached-eddy Simulation, Resistant to Ambiguous Grid Densities," Theoretical and Computational Fluid Dynamics, Vol. 20, (3), May 2006, pp. 181. DOI: 10.1007/s00162-006-0015-0.

6. J. Letzgus, High-Fidelity Simulation of Dynamic Stall on Helicopter Rotors, Ph.D. thesis, Institute of Aerodynamics and Gas DynamicsUniversity of Stuttgart, 2021.

7. J. Letzgus, M. Keßler, and E. Krämer, "Simulation of Dynamic Stall on an Elastic Rotor in High-Speed Turn Flight," Proceedings of the 75th Annual Forum, May 2019.

8. F. Richez, R. Jain, M. Smith, A. Grubb, and C. Castells, "Validation and Analysis of Aeroelastic Simulations of the UH-60A Rotor from Pre-to Poststall Flight Conditions," 76th Annual Forum & Technology Display (Vertical Flight Society), October 2020.

9. P. Sridhar, A. Crawford, and M. J. Smith, "Sensitivity of rotor aeroelastic predictions with two-equation turbulence models," CEAS Aeronautical Journal, 2024. DOI: 10.1007/s13272-024-00797-9.

10. N. M. Chaderjian, "A Quantitative Approach for the Accurate CFD Simulation of Hover in Turbulent Flow," Journal of the American Helicopter Society, Vol. 68, (4), 2023, pp. 42009–42028. DOI: 10.4050/JAHS.68.042009.

11. C. C. Wolf, A. Weiss, C. Schwarz, J. Braukmann, S. Koch, and M. Raffel, "Wake Unsteadiness and Tip Vortex System of Full-Scale Helicopters in Ground Effect," Journal of the American Helicopter Society, Vol. 67, (1), 2022, pp. 1–17. DOI: 10.4050/JAHS.67.012010.

12. A. Bodling, C. Schwarz, C. Wolf, and A. Gardner, “Numerical and Experimental Assessment of Parameters Influencing the Development of Secondary Vortex Structures in Rotor Wakes,” 79th Annual Forum of The Vertical Flight Society, 2023.

13. Z. Lietzau, M. Ramasamy, R. Jain, J. G. Leishman, and J. Ekaterinaris, “Comparison of Advanced RANS Modeling with Dual-Plane PIV Measurements for a Hovering Rotor,” AHS International 73rd Annual Forum, 2017.

14. F. R. Menter, M. Kuntz, and R. Langtry , “Ten years of industrial experience with the SST turbulence model,” Heat and Mass Transfer, Vol. 4, (1), 2003, pp. 625–633. DOI: 10.1.1.460.2814.

15. J. Dacles-Mariani, D. Kwak, and G. Zilliac, “On numerical errors and turbulence modeling in tip vortex flow prediction,” International Journal for Numerical Methods in Fluids, Vol. 30, (1), 1999, pp. 65–82. DOI: 10.1002/(SICI)1097-0363(19990515)30:1<65::AID-FLD839>3.0.CO;2-Y.

16. M. L. Shur, M. K. Strelets, A. K. Travin, and P. R. Spalart, “Turbulence Modeling in Rotating and Curved Channels: Assessing the Spalart-Shur Correction,” AIAA Journal, Vol. 38, (5), 2000, pp. 784–792. DOI: 10.2514/2.1058.

17. F. Richez, and Rohit Jain, “Prediction of the laminar-to-turbulent transition position on a helicopter rotorblade with cyclic pitch variation,” Vertical Flight Society’s 79th Annual Forum & Technology Display, 2023.

18. B. G. van der Wall, “Impact of Rotor Inflow Modeling on Maximum Thrust, and Beyond, of an Isolated Rotor in Hover,” 50th European Rotorcraft Forum (in Scopus), September 2024.

19. B. G. van der Wall, J. W. Lim, Joon, J. Riemenschneider, S. Kalow, G. A. Wilke, D. D. Boyd, J. Bailly, Y. Delrieux, I. Cafarelli, Y. Tanabe, H. Sugawara, S. N. Jung, S. H. Hong, Seong, D.-H. Kim, H. J. Kang, G. Barakos, R. Steininger, “New smart twisting active rotor (STAR): pretest predictions,” CEAS Aeronautical Journal, 2024. DOI: 10.1007/s13272-024-00731-z.

20. R. Gerlach, “Untersuchung der aerodynamischen Eigenschaften des HART-II Hubschrauberrotors im Schwebeflug mittels CFD-Simulationen,” , April 2024.

21. B. G. van der Wall, “A Comprehensive Rotary-Wing Data Base for Code Validation: The HART II International Workshop,” The Aeronautical Journal, Vol. 115, (1164), 2011, pp. 91–102.

22. J. Raddatz, and J. K. Fassbender, “Block Structured Navier-Stokes Solver FLOWer,” MEGAFLOW - Numerical Flow Simulation for Aircraft Design, edited by N. Kroll and J. K. Fassbender, 2005.

23. K. Kitamura, and E. Shima, “Towards shock-stable and accurate hypersonic heating computations: A new pressure flux for AUSM-family schemes,” Journal of Computational Physics, Vol. 245, 2013, pp. 62–83. DOI: 10.1016/j.jcp.2013.02.046.

24. Y. Tanabe, S. Saito, and H. Sugawara, “Validation of High Resolution CFD Analysis For Flowfield Around a Rotor,” The 40th Japan Society for Aeronautical and Space Sciences Annual Meeting, 2009.

25. S. Yamamoto, and H. Daiguji, “Higher-order-accurate upwind schemes for solving the compressible Euler and Navier-Stokes equations,” Computers & Fluids, Vol. 22, (2-3), 1993, pp. 259–270. DOI: https://doi.org/10.1016/0045-7930(93)90058-H.

26. G. D. van Albada, B. van Leer, and W. W. Roberts Jr., “A comparative study of computational methods in cosmic gas dynamics,” Astronomy and Astrophysics, Vol. 108, (1), 1982, pp. 76–84.

27. G. Wilke, “Comparisons of Different Spatial Schemes and Limiters for Helicopter Flows,” New Results in Numerical and Experimental Fluid Mechanics XIII, edited by A. Dillmann, G. Heller, E. Krämer, and C. Wagner, 2021. DOI: 10.1007/978-3-030-79561-0.

28. S. Yoon, and A. Jameson, “Lower-upper Symmetric-Gauss-Seidel method for the Euler and Navier-Stokes equations,” AIAA Journal, Vol. 26, (9), 1988, pp. 1025–1026. DOI: 10.2514/3.10007.

29. V. Vatsa, M. Carpenter, and D. Lockard, “Re-evaluation of an Optimized Second Order Backward Difference (BDF2OPT) Scheme for Unsteady Flow Applications,” 48th AIAA Aerospace Sciences Meeting Including the New Horizons Forum and Aerospace Exposition, 2010. DOI: 10.2514/6.2010-122.

30. R. Radespiel, C. Rossow, and R. C. Swanson, “Efficient cell-vertex multigrid scheme for the three-dimensional Navier-Stokes equations,” AIAA Journal, Vol. 28, (8), 1990, pp. 1464–1472. DOI: 10.2514/3.25239.

31. R. Radespiel and N. Kroll, “Accurate Flux Vector Splitting for Shocks and Shear Layers,” Journal of Computational Physics, Vol. 121, (1), 1995, pp. 66–78. DOI: https://doi.org/10.1006/jcph.1995.1179.

32. P. R. Spalart, "On the flow field induced by a hovering rotor or a static jet," Journal of Fluid Mechanics, Vol. 701, 2012, pp. 473–481. DOI: 10.1017/jfm.2012.188.

33. H. Dol, J. Kok, and B. Oskam, "Turbulence modelling for leading-edge vortex flows," 40th AIAA Aerospace Sciences Meeting Exhibit, 2002. DOI: 10.2514/6.2002-843.

34. J. C. Kok, "Resolving the Dependence on Freestream Values for the k- Turbulence Model," AIAA Journal, Vol. 38, (7), 2000, pp. 1292–1295. DOI: 10.2514/2.1101.

35. M. S. Gritskevich, A. V. Garbaruk, Andrey, J. Schütze, and F. R. Menter, "Development of DDES and IDDES Formulations for the k- Shear Stress Transport Model," Flow, Turbulence and Combustion, Vol. 88, (3), 2012, pp. 431–449. DOI: 10.1007/s10494-011-9378-4.

36. C. C. Heister, "A Method for Approximate Prediction of Laminar-Turbulent Transition on Helicopter Rotors," Journal of the American Helicopter Society, Vol. 63, (3), July 2018, pp. 1–14.

37. P. Beaumier, E. Chelli, and K. Pahlke, "Navier-Stokes Prediction of Helicopter Rotor Performance in Hover Including Aeroelastic Effects," 56th Annual Forum of the American Helicopters Society, 2000.

38. F. Jia, Q. Wang, and P. Spalart, "Improved Initial and Boundary Conditions for Hovering Rotor CFD Simulations," Vertical Flight Society's 78th Annual Forum & Technology Display, May 2022.

39. Whitfield, D., Three-dimensional unsteady Euler equations solution using flux vector splitting, 1984. DOI: 10.2514/6.1984-1552.

40. T. Schwarz, Ein blockstrukturiertes Verfahren zur Simulation der Umströmung komplexer Konfigurationen, Ph.D. thesis, Institut für Aerodynamik und Strömungstechnik, DLR, Braunschweig, 2005.

41. G. Wilke, Aerodynamic Optimization of Helicopter Rotorblades using Variable Fidelity Methods, Ph.D. thesis, Technische Universität Braunschweig, 2017.

42. C. B. Allen, "CHIMERA volume grid generation within the EROS code," Proceedings of the Institution of Mechanical Engineers, Part G: Journal of Aerospace Engineering, Vol. 214, 2000, pp. 125–140. DOI: 10.1243/0954410001531962.

43. G. Wilke, "Quieter and Greener Rotorcraft: Concurrent Aerodynamic and Acoustic Optimization," CEAS Aeronautical Journal, Vol. 12, (1), 2021, pp. 495–508. DOI: 10.1007/s13272-021-00513-x.

44. Y. Hong, G. Wilke, and W. Khier, "Improved SA Turbulence Model For Hovering Rotor Using Production Limiter," 51st European Rotorcraft Forum, September 2025.

45. P. R. Spalart, "Young-Person's Guide to Detached-Eddy Simulation Grids," Technical report, NASA, 2001.

46. S. Yoon, N. Chaderjian, T. H. Pulliam, and T. Holst, Effect of Turbulence Modeling on Hovering Rotor Flows, 2015. DOI: 10.2514/6.2015-2766.